Research Square

Preprints are preliminary reports that have not undergone peer review.
They should not be considered conclusive, used to inform clinical practice,
or referenced by the media as validated information.

Microstructure and mechanical properties comparison in MIG-welded 6082 produced with heat-treatable TiB containing filler metal and conventional aluminum filler metals

Amir Khodabakhshi

amir.khodabakhshi@lut.fi

Lappeenranta University of Technology: LUT University

Shahriar Afkhami

LUT-yliopisto: LUT University

Hamidreza Rohani Raftar

Fraunhofer Institute for Mechanics of Materials IWM: Fraunhofer-Institut fur Werkstoffmechanik IWM

Ville Laitinen

LUT School of Engineering Science

Sakari Penttilä

LUT School of Energy Systems

Tuomas Skriko

LUT School of Energy Systems

Research Article

Keywords: Microstructure, Mechanical properties, MIG welding, Aluminum alloy, Finite element simulation.

Posted Date: September 24th, 2026

DOI: https://doi.org/10.21203/rs.3.rs-10947618/v1

License: This work is licensed under a Creative Commons Attribution 4.0 International License.
Read Full License

Microstructure and mechanical properties comparison in MIG-welded 6082 produced with heat-treatable TiB containing filler metal and conventional aluminum filler metals

Amir Khodabakhshi [a,*], Shahriar Afkhami [a], Hamidreza Rohani Raftar [b, d], Ville Laitinen [c], Sakari Penttilä [a], Tuomas Skriko [a]

a. Laboratory of Welding Technology, LUT University, Lappeenranta, Finland.
b. Steel Structures, School of Energy Systems, LUT University, Lappeenranta, Finland.
c. Department of Physics, School of Engineering Sciences, LUT University, Lappeenranta, Finland.
d. Fraunhofer Institute for Mechanics of Materials IWM, Woehlerstraße 11, Freiburg, Germany.

Abstract

Using different filler materials in aluminum welding can improve the mechanical properties of the weld zone. In this study, a 6063 heat-treatable filler containing TiB particles was used, and the resulting weld joint's microstructure and mechanical properties were compared with those obtained using conventional 5356 and 4043 fillers. A dynamic wire movement system was applied to reduce the welding heat input and improve the grain size of the weld material. A validated finite element model was also employed to investigate the weld thermal cycle under two welding conditions. The presence of porosity and other defects was examined using X-ray computed tomography. The microstructures of the weld zone in different samples were analyzed and compared using a scanning electron microscope equipped with electron backscatter diffraction and energy-dispersive X-ray spectroscopy. Mechanical properties of the weld joint were evaluated through hardness testing and tensile testing equipped with digital image correlation. The results showed that in samples welded with the heat-treatable filler, the grain size of the weld zone was significantly reduced. However, the dynamic arc welding system alone did not produce a comparable reduction in grain size. Despite grain refinement, the weld zone's hardness with 6063 heat-treatable filler was lower than that with conventional fillers. These samples generally failed along the fusion line region. Overall, this study showed that 6063 filler is sensitive to gas porosity and shrinkage cavity formation, as well as a greater reduction in the mechanical properties of the weld metal.

Keywords

Microstructure, Mechanical properties, MIG welding, Aluminum alloy, Finite element simulation.

* Corresponding author.
Amir Khodabakhshi, PhD student and Researcher,
E-mail address: amir.khodabakhshi@lut.fi
Welding Laboratory, School of Energy Systems, LUT University, P.O. Box 20, FI-53851, Lappeenranta, FINLAND

1. Introduction

6082 aluminum alloy is used in various industrial sectors, including structural components, primarily due to its favorable combination of mechanical properties, corrosion resistance, and formability. It is considered a potential replacement for some steel parts in automotive applications, such as rod ends, because it can withstand shock and vibration loads without requiring design changes [1]. Its use in lightweight vehicles and energy-efficient construction also contributes to lower carbon emissions and facilitates the advancement of sustainable urban environments [2]. Sometimes, welding aluminum alloys is unavoidable for these manufacturing components. Effective welding techniques are required to ensure mechanical performance and structural reliability [3]. metal inert gas (MIG) welding is a commonly employed method for 6xxx series aluminum alloys, valued for its reasonable quality and production rate. In MIG welding, shielding gases such as argon and helium protect the weld bead from contamination, which is essential for maintaining weld integrity. Process parameters, including welding current and gas flow rate, significantly influence weld tensile strength and hardness. Accordingly, optimization techniques have been applied to determine the best welding conditions for 6xxx series alloys. Further, filler materials like 4043 are commonly used to minimize stress cracking during welding. Additionally, MIG welding is used for 6xxx series alloys, often with filler metals like Al-5Mg (AA5356), to enhance the mechanical properties and microstructural characteristics of the welds. Microstructural studies using optical and scanning electron microscopy have been conducted to evaluate the effects of these welding techniques on the alloys [4].

Such studies showed that MIG welding of 6xxx series aluminum alloys presents several challenges related to microstructural control and mechanical properties. One key issue is the influence of welding heat input on weld metal microstructure and softening in the heat-affected zone (HAZ) [4]. The microstructure of the weld metal zone (WMZ) in 6xxx alloys is also affected by the welding current. At lower currents, the molten pool exhibits a single circulation pattern, while higher currents induce multiple circulations, which influence grain structure. The grain morphology transitions from fine equiaxed grains to coarser grains as current increases, with the proportion of high-angle grain boundaries peaking at an intermediate current [5].

The choice of filler metal and welding technique also impacts microstructure and mechanical properties. Studies on 6XXX series alloys welded by both TIG and MIG methods highlight the importance of filler composition, such as Al-5Mg (AA5356), in achieving the desired hardness and microstructural characteristics [6, 7]. Studies on 6061 and 7020 alloys with specific filler metals (e.g., Al-5Mg) highlight the importance of matching filler composition to the base metal to optimize the resultant hardness and microstructure [8].

Recently, many researchers have tried to control the microstructure through alloying additions to produce finer, equiaxed grains, which improve the weld's mechanical performance [9, 10]. This grain modification is most notably achieved by adding grain refiners to the weld metal. These refiners typically contain elements such as titanium and boron, which promote nucleation during solidification, leading to a transition from columnar to equiaxed grain structures and a significant reduction in mean grain size [11]. Grain refinement can also be achieved by changing the chemical composition of filler wires to form compounds such as $TiBr_4$, TiB_2, and TiC, which act as nucleation sites during solidification [12]. The presence of intermetallic phases such as Al_3Ti has also been identified as critical for nucleation and grain size reduction.

Technological advancements in welding methods, such as low-energy MIG welding techniques (Cold Arc and CMT), have demonstrated the feasibility of producing high-quality and acceptable joints in aluminum alloys. These methods help address the challenges of

welding thin aluminum alloy plates, making welding a practical process in production [13]. This process is based on the mechanical droplet detachment method, which differs from conventional arc welding classifications, allowing precise control over metal transfer and reducing heat input applied to the base material [14, 15].

For example, Wei et al. [16] showed that CMT welds exhibited improved hardness and tensile strength relative to MIG welds, as the reported hardness values are 103.9 HV for CMT weld zones and 92.6 HV for MIG welds in the same Al-Zn-Mg-Cu-Er-Zr alloy. Tensile strength was also higher in CMT joints (334.0 MPa) than in MIG joints (270.3 MPa). Cornacchia et al. [17] also report that similar trends were observed in studies on 6005A-T6 aluminum alloy, where CMT and fiber laser-MIG hybrid welds demonstrated superior mechanical properties, including hardness and tensile strength, compared to traditional MIG welds.

According to the literature, despite the generally favorable performance of the Cold Metal Transfer (CMT) welding process, several inherent limitations must be considered. The combination of rapid cooling rates and the development of internal stress can increase susceptibility to pore formation and solidification cracking, particularly at higher welding speeds. Also, in lap joint configurations, the elongation of the arc significantly raises the risk of incomplete fusion, which can compromise joint integrity. Further, although CMT's reduced heat input minimizes spatter and allows welding of thin sheet materials, it does not fully prevent metallurgical degradation in heat-treatable aluminum alloys. Similar to conventional fusion welding processes, CMT causes a partial loss of the precipitation strengthening mechanism in alloys such as the 6xxx and 7xxx series, leading to the formation of a softened zone characterized by reduced hardness and yield strength, as reported in previous studies [18].

Extensive research has investigated the effects of different filler metals and the application of CMT-based processes for welding precipitation-hardened aluminum alloys. However, the specific use of a heat-treatable filler metal containing particles that modify grains remains comparatively underexplored. Accordingly, in this study, besides using a 6063 filler material containing TiB to weld AA6082 alloy, welding was carried out using the EWM React process, which employs controlled mechanical wire motion to promote stable droplet detachment. This approach, functionally similar to CMT, reduces heat input while improving arc stability, making it a promising route for joining precipitation-hardening aluminum alloys with potentially improved control over weld metal and HAZ responses.

The primary objective of this study is to investigate the combined use of a low heat input, controlled metal-transfer welding approach and a heat-treatable filler metal containing TiB for welding aluminum alloys. To assess the effectiveness of these two approaches, the 6063 filler and the CMT process are systematically compared against conventional filler metals and a conventional MIG welding method. The work focuses on establishing clear process–structure–property relationships by evaluating both microstructural investigations and the mechanical performance of the welded joints. By this comparative assessment, this study intends to address the existing research gap and offer practical guidance for improving the weld quality of 6082 aluminum alloy.

2. Experimental Procedures

2.1. Materials and Welding Procedures

The base material investigated in this study was AA6082, in the T651 condition, as rolled plates. The nominal chemical composition of the base material, obtained from the manufacturer's material certificate, is presented in Table 1. Welding was carried out using 1.2 mm diameter filler wires. The chemical compositions of the filler materials are also

summarized in Table 1. Additionally, the mechanical properties of the base material and filler wires are listed in Table 2.

Table 1: Chemical composition.

6082 (AlSi1MgMn)-T651	0.80	1.00	0.42	0.42	0.02	-
ER 6063 (AlMg0,7SiTiB)	0.45 - 0.90	0.20 - 0.60	< 0.35	< 0.10	0.20 – 0.30	0.04 – 0.06
ER 5356 (AlMg5Cr)	4.50 – 5.50	< 0.25	0.40	0.05 – 0.20	0.06 – 0.20	-
ER 4043 (AlSi5)	< 0.20	4.50 – 5.50	< 0.60	< 0.15	< 0.15	-

Table 2: Mechanical properties of the base material and filler wires.

6082 (ALSI1MGMN)-T651	290	340	20
ER 6063 (ALMG0,7SITIB)	200 - 260	250 - 280	6 - 12
ER 5356 (ALMG5)	120	250	18
ER 4043 (ALSI5)	70	140	4

Before welding, the plates were cut to 300×110×4 mm and prepared with a square butt joint configuration with a 2 mm air gap. Fig. 1 shows a schematic illustration of the joint geometry and specimen dimensions.

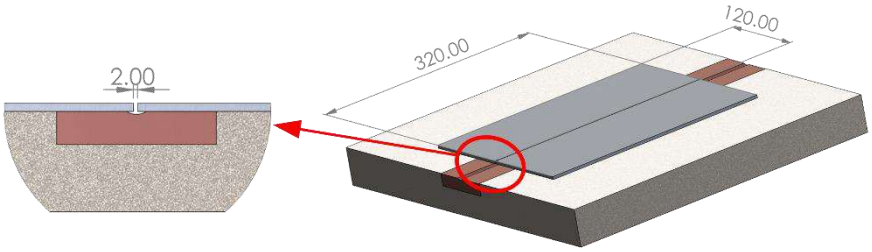


Fig. 1: Schematic illustration of the joint design, groove geometry, and specimen dimensions.

Welding was carried out using the MIG process with a robotized setup. An EWM welding power source equipped with a reversing actively controlled transfer system was used. The welding parameters were selected based on preliminary trial welds to achieve stable arc behavior and fully penetrated joints. Sample codes and their variables, including welding current, arc voltage, welding speed, and wire feed speed, along with other parameters employed in this work, are given in Table 3.

Table 3: Welding process parameters used in this study.

Sample	Welding current (I)	Welding voltage (V)	Welding speed (m/min)	Welding mode	Wire feed speed (m/min)	Heat input (kJ/mm)	Constant parameters
W6N	154	16.5	10	Normal	8.4	0.229	torch angle = 2° (pulling) contact-tip-to-work distance = 18 mm Argon flow rate = 15 L/min
W6R	150	13.8	10	CMT	7.9	0.186	
W5N	145	17.0	10	Normal	10.0	0.222	
W5R	150	13.2	10	CMT	9.7	0.178	
W4N	170	19.0	10	Normal	8.2	0.291	
W4R	130	14.0	8	CMT	6.8	0.205	

2.2. Finite Element Thermal Simulation

A finite element model (FEM) was developed in Simufact Welding software 2024.3. version to simulate and compare the welding thermal cycles of the W6N and W6R specimens. These samples were selected because both specimens were welded using the same TiB-containing 6063 filler metal but under normal and CMT welding conditions, respectively. Therefore, their

comparison allowed the effect of welding mode to be examined and provided a representative comparison between normal and CMT welding modes. The numerical analysis was limited to these two representative specimens because simulating all six welding conditions would have substantially increased the computational time without providing additional information necessary for the specific purpose of this thermal comparison.

The predicted temperature histories were validated against experimental measurements. Five K-type thermocouples were attached to each specimen to record temperature variations during welding and subsequent cooling. After welding, a profilometer measurement system was used to determine the exact thermocouple locations. These coordinates were then used to extract the numerical temperature histories from the corresponding locations in the finite element models, allowing a direct comparison between the experimental and simulation results.

The welded joint was simulated using a three-dimensional finite element mesh, as shown in Fig. 2. Local mesh refinement was applied near the plate edge and joint region to capture the steep temperature gradients generated by the moving heat source. The model was discretized using eight-node linear hexahedral (CHEXA) solid elements. The nominal element size was approximately 0.5 mm in the weld bead and approximately 1 mm in the adjacent refined plate region. The element size was gradually increased through the transition region, reaching approximately 3 mm in the coarse regions farther from the weld. A gradually coarser mesh was applied farther from the joint, where lower temperature gradients were anticipated.

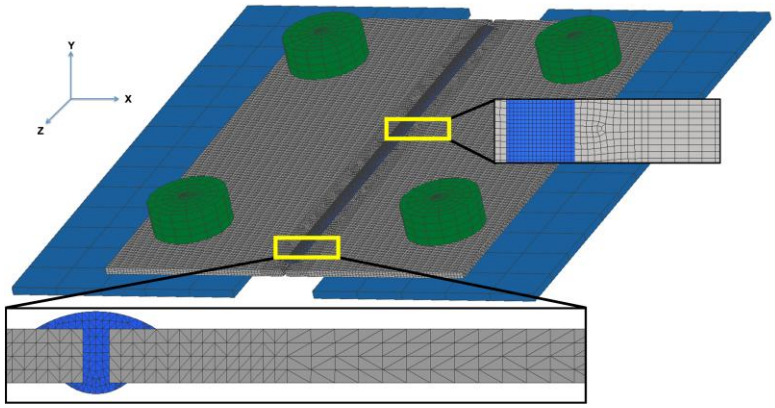
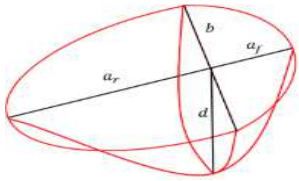


Fig. 2: Finite element model of the welded joint, including the clamping configuration and the locally refined mesh along the weld path.

The welding heat source was represented using Goldak's double-ellipsoidal heat source model. The main geometrical parameters, Gaussian parameters, and heat-scaling factors used for the W6N and W6R models are summarized in Table 4. The heat source dimensions were calibrated separately for the two welding conditions to reproduce the corresponding experimental thermal cycles and weld geometries. The model's initial temperature and the ambient temperature were both set to 20 °C. Heat loss from the exposed surfaces was represented by convection and thermal radiation. A constant convective heat-transfer coefficient of 20 W m^{-2} K^{-1} and a constant surface emissivity of 0.2 were applied. Heat transfer across the contacting surfaces was represented using a constant contact heat-transfer coefficient of 100 W m^{-2} K^{-1}. A heat source efficiency of 0.90 and 0.8 was used for W6N and W6R, respectively. The thermophysical properties of the 6082 base material were obtained from the Simufact material library and used without modification. Further details regarding the heat

source formulation and its parameters are provided in a previous study involving a comparable welding configuration for aluminum alloy joints [19].

Table 4: Main parameters of the Goldak double-ellipsoidal heat source used in the W6N and W6R thermal models.

Goldak double-ellipsoidal heat source	Heat source parameter	W6N	W6R
	Front length, a_f(mm)	2.0	2.5
	Rear length, a_r(mm)	7.0	4.0
	Width, b(mm)	3.8	3.0
	Depth, d(mm)	5.7	6.0
	Gaussian parameter, M	1.0	1.0
	Front heat-scaling factor, f_f	0.444	0.769
	Rear heat-scaling factor, f_r	1.556	1.231

2.3. Materials Characterization and Mechanical Testing

After welding, cross-sectional specimens were cut from the mid-length of each welded joint. The samples were mounted, ground using SiC abrasive papers from 250 to 2000 grit sizes, and polished using diamond suspensions down to 1 μm to obtain a mirror-like surface finish. The samples were then subjected to a final polishing step using a 0.04 μm alumina colloid. The samples were chemically etched using Weck's reagent to reveal microstructural features. Further characterization was conducted using an optical microscope and a scanning electron microscope (SEM) equipped with energy-dispersive X-ray spectroscopy (EDS). Electron backscatter diffraction (EBSD) was also employed to characterize the crystallographic orientation, grain size, and grain boundaries. For EBSD analysis, the specimens were prepared using an electrolytic polishing process to obtain a strain-free surface suitable for crystallographic characterization. Electropolishing was carried out using an electrolyte containing ethanol (60.0–78.4%), butoxyethanol (9.2–13.8%), perchloric acid (4.7–<10%), and water (4.6–13.8%). The electropolishing procedure was performed at room temperature with an applied voltage of 25 V for a duration of 30 s. Phase identification was carried out using X-ray diffraction (XRD) analysis. XRD measurements were performed on selected regions, including the base material and weld metal, using X-ray diffraction with Co Kα radiation (λ = 1.78901 Å). Fig. 3 shows a schematic cross-section of the welded joint and indicates the locations selected for different analyses, including metallography, SEM, EBSD, hardness measurements, and XRD samples.

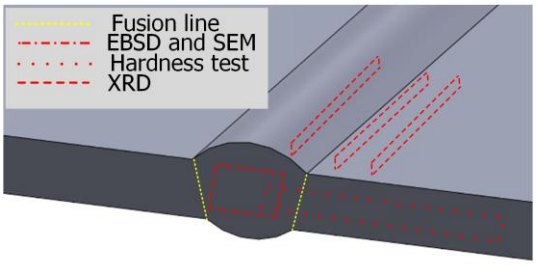


Fig. 3: Schematic cross-section showing the sampling locations for metallography, SEM, EBSD, hardness measurements, and XRD

Quasi-static tensile tests were conducted at room temperature using a universal testing machine. Tensile specimens, Fig. 4a, were extracted from the welded joints with the loading direction perpendicular to the welding direction. For each experimental condition, at least three

specimens were tested, and the average values were reported. Digital image correlation (DIC) was employed during tensile testing to obtain full-field strain distributions and local deformation behavior. DIC analysis was performed using ZEISS ARAMIS to evaluate strain localization and strain evolution. Following tensile testing, fracture surfaces were examined using SEM to identify the dominant fracture mechanisms and correlate them with the microstructural features.

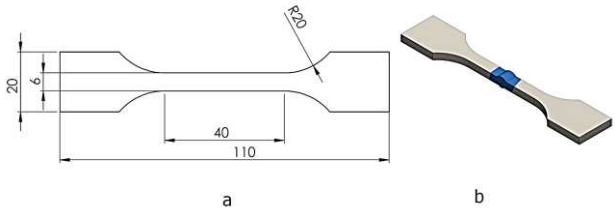


Fig. 4: Tensile test specimen, a) Geometry of the specimen, b) XCT analysis area.

Before tensile testing, micro X-ray computed tomography (XCT) was used to characterize the 3D distribution, morphology, and volume fraction of internal porosity in the welded joints extracted from the tensile test samples. The XCT analysis was performed in the area indicated in Fig. 4b using a Phoenix Microme |NEO system (Waygate Technologies). The scans were conducted with a voxel size of 10 µm resolution. Image reconstruction and defect segmentation were carried out using VGSTUDIO MAX software. A consistent threshold-based segmentation approach was applied to distinguish pores from the surrounding material. Fig. 5 shows the XCT experimental setup, including the X-ray source and the tensile specimen mounted in the sample holder during scanning. The detector is located below the scanning stage and is therefore not visible in the image

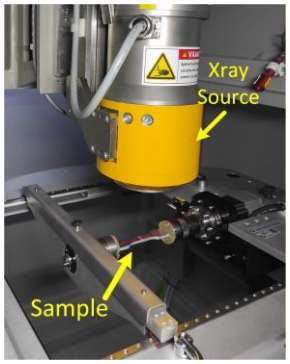


Fig. 5: Setup for XCT, showing the X-ray source and the mounted sample during scanning.

Vickers measurements were performed on polished transverse cross-sections using the Struers DuraScan 70 hardness test machine according to ASTM E384. A test load of 200 g (HV0.2) with a dwell time of 10 s was applied. Indentations were placed along one horizontal line to measure linear profile hardness values.

3. Results

The welded joints were first examined to evaluate the overall weld appearance, bead geometry, and macrostructural features. All welding conditions produced continuous weld beads without visible surface cracking. However, weld bead shape and weld metal geometry differed depending on the material and welding mode. One approach to examine the effect of the CMT and normal welding modes is to conduct a FEM simulation to estimate the thermal cycle. First, it was necessary to validate the accuracy of the FEM thermal analysis. Fig. 6

compares the experimental temperature histories recorded by thermocouples attached to the plate surfaces with the corresponding FEM results obtained for samples W6N and W6R. Fig. 6a presents the normal welding condition in sample W6N, where TC1 and TC2 were located at 0.70 mm and 2.35 mm from the weld toe, respectively. The peak temperatures recorded experimentally at TC1 and TC2 were approximately 543 °C and 428 °C, while the corresponding FEM predictions were approximately 549 °C and 426 °C. Fig. 6b presents the CMT welding condition in sample W6R, where TC1 and TC2 were located 0.50 mm and 1.51 mm from the weld toe, respectively. In this condition, the experimental peak temperatures at TC1 and TC2 were approximately 553 °C and 497 °C, compared with FEM predictions of approximately 576 °C and 518 °C. Overall, the FEM results reproduced both the rapid heating stage and the subsequent cooling behavior observed experimentally. The difference between the experimental and predicted peak temperatures remained below approximately 10%, indicating acceptable agreement between the FEM analysis and the experimental measurements. The validated FEM model was therefore used to further examine the thermal behavior of the welded joints. Fig. 6c and 6d show the thermal gradient results for the welded joint. The isothermal contour qualitatively matches the penetration profile, HAZ, and fusion line, as verified through micro-sample observations.

The use of the CMT welding mode affected the weld bead formation by modifying the metal transfer behavior and reducing the effective heat input. As a result, differences in weld width, penetration profile, and weld reinforcement were observed between the conventional and CMT welding conditions. These differences indicate that both filler composition and controlled wire motion influenced the solidification behavior and final weld geometry.

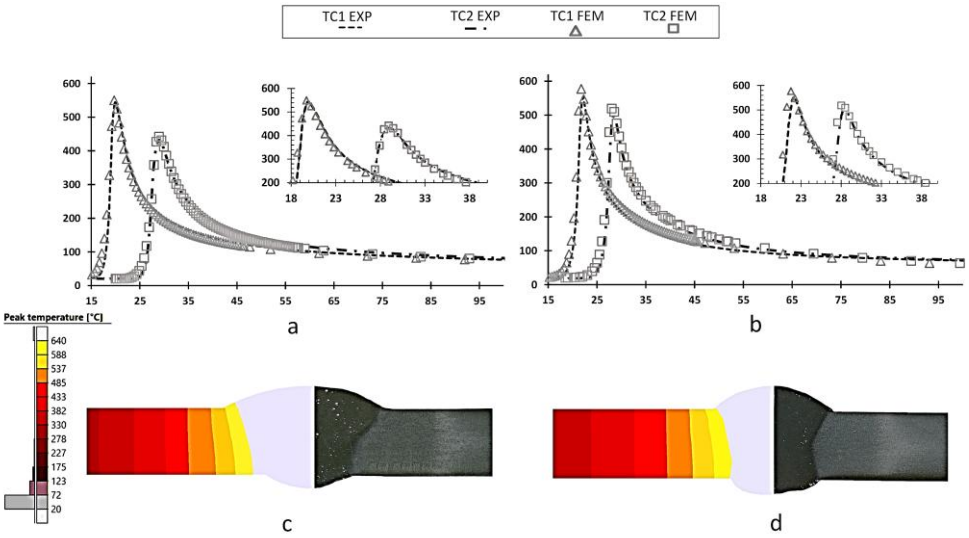


Fig. 6: Comparison of the experimental and FEM-predicted thermal cycle for samples a) W6N, b) W6R, and isothermal contour for samples c) W6N, and d) W6R.

Fig. 7 shows the macrograph and weld-geometry values for the investigated welded joints. Fig. 7a and 7b present the cross-sections of W5N and W5R, respectively. Both samples show full penetration and a continuous fusion zone. However, a clear difference in weld geometry can be observed between the normal and CMT welding conditions. The W5N sample has a wider weld bead and a larger weld zone area compared with W5R. This indicates that the CMT welding mode reduced the effective weld size for the 5356 filler condition. A similar trend is also observed for the weld bead width and weld zone area across all samples, as shown in Fig. 7c. In general, the CMT welding mode reduced the weld zone area compared with the corresponding normal welding condition for the same filler material. This behavior can be

related to the controlled metal transfer and lower effective heat input in the CMT process. Weld geometry is important because it can affect the local stress concentration and, therefore, the mechanical performance of the weld joint [7].

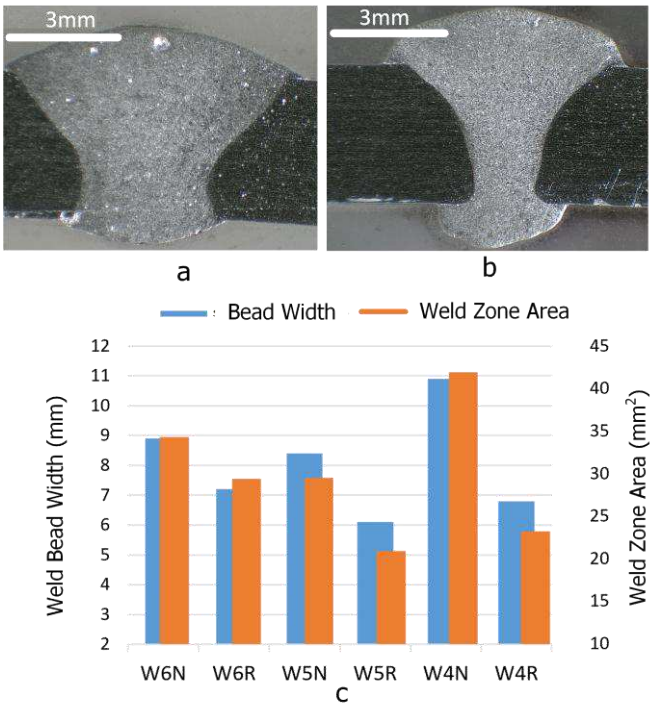


Fig. 7: Weld geometry and macrostructural characteristics of samples a) W5N and b) W5R, along with c) a comparison of weld bead width and weld zone area for all samples.

The validated FEM results also support the reduction in weld heat input produced by the CMT welding mode. Fig. 8 presents the simulated temperature profiles as a function of distance from the weld bead center for samples W6N and W6R. At the weld bead center, both samples reached similar maximum temperatures of approximately 710 °C. In both cases, the maximum temperature decreased with increasing distance from the weld bead center. However, the maximum temperature decreased more rapidly in W6R compared to W6N. This result indicates that the CMT welding mode produced a narrower high-temperature region around the weld bead, which is consistent with the smaller weld bead dimensions and weld zone area observed for W6R.

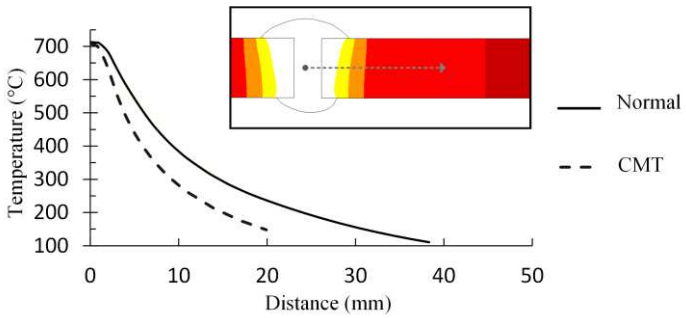


Fig. 8: FEM temperature profiles from the weld bead center to the base metal for samples W6N and W6R.

Fig. 9 displays the XCT results of welded joints created under various welding conditions. The detected internal imperfections in the weld region are shown with different colors according to their equivalent diameter. The XCT results show clear differences among the samples' imperfections. Additionally, a common feature in all XCT images was the presence of many small cavities. Most of these cavities had diameters below 0.2 mm and are shown in blue. Samples W5N and W5R contained a lower number of detected internal imperfections compared with the other samples. This suggests that using 5356 filler reduced the tendency for void formation. In contrast, the other welded samples showed a higher number of detected imperfections within the weld region. According to ISO 10042 [20], the maximum acceptable dimension of a single gas pore depends on the quality level and should be less than 0.1 to 0.3 times the plate thickness. Since the plate thickness in this study was 4 mm, the acceptable maximum pore diameter is approximately 0.4 mm for quality level B (highest quality) and 0.8 mm for quality level C (medium quality). Therefore, most of the small cavities detected by XCT were below the critical size limit for individual gas pores.

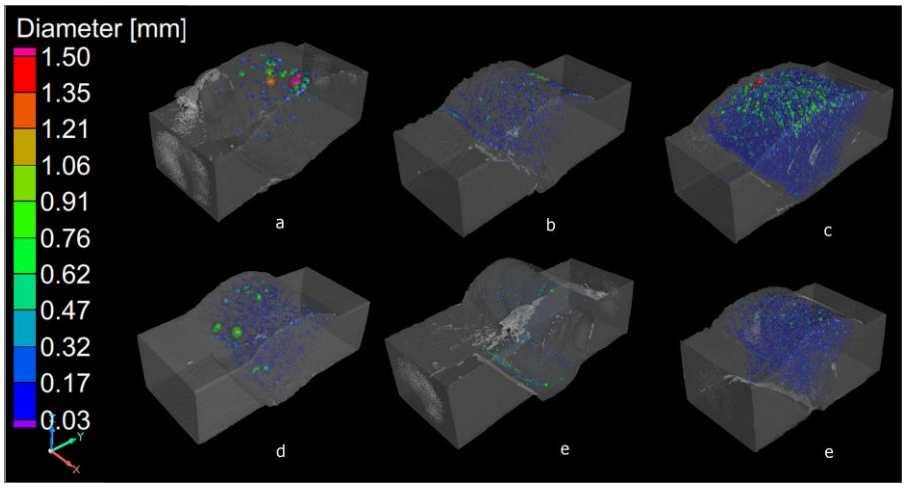


Fig. 9: 3D XCT visualization of internal imperfections in the welded joints: a) W6N, b) W5N, c) W4N, d) W6R, e) W5R, and f) W4R.

Microscopic observations showed that the small cavities detected by XCT could correspond to both gas pores and shrinkage cavities. Fig. 10 shows SEM images from the weld region of sample W4N. In Fig. 10a, several pores with a nearly spherical morphology can be observed. These rounded cavities are typical of gas porosity. At higher magnification, smaller cavities with irregular shapes were also observed between the spherical pores, as shown in Fig. 10b. These irregularly shaped cavities are more likely related to shrinkage during solidification rather than gas pores. Unlike gas pores, shrinkage cavities are not fully spherical because they form during the final stages of weld metal solidification.

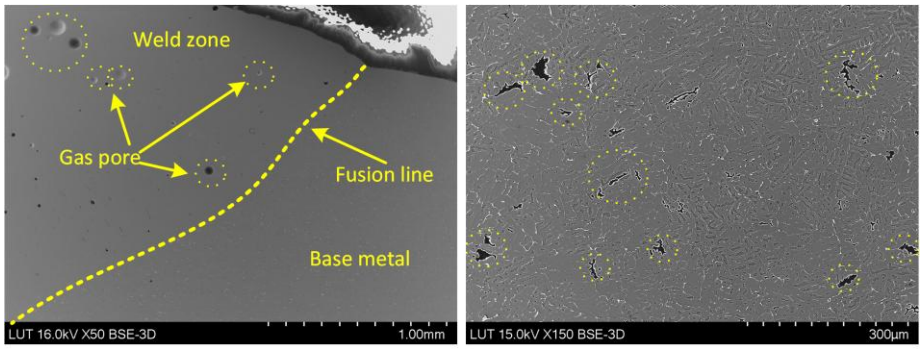


Fig. 10: SEM images of internal cavities observed in the weld region of sample W4N: a) spherical gas pores and b) irregular shrinkage cavities formed during solidification.

Fig. 11 shows the EBSD inverse pole figure (IPF) maps of the weld metal regions for the different welding conditions. Clear differences in grain structure can be observed between the samples. The weld metals in Fig. 11a and Fig. 11d (samples W6N and W6R, respectively) exhibit a finer, more equiaxed grain structure than the other conditions. The finer grain structure observed in Fig. 11a and Fig. 11d indicates that grain refinement was more effective in these welding conditions. Although the CMT welding process was used for sample W5R and W4R (Fig. 11e and 11f) to reduce the heat input, it did not lead to a comparable reduction in grain size for the other two filler materials. Therefore, the observed grain refinement appears to be mainly related to the presence of TiB particles in the filler metal rather than only to the reduction in heat input. Fig. 12 presents the average equivalent grain diameter and the number of detected grains for the different samples. The quantitative results follow the same trend as the EBSD maps. Samples W6N and W6R showed a higher number of detected grains and a smaller average equivalent grain diameter compared with the other samples.

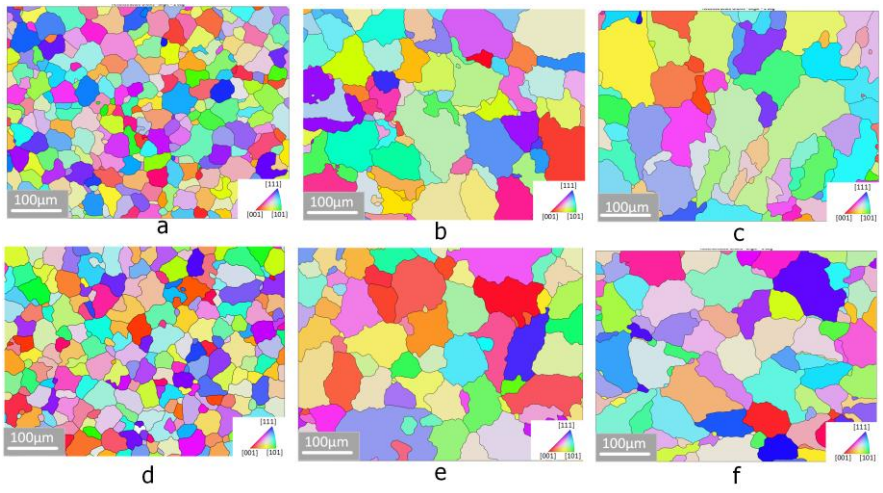


Fig. 11: EBSD maps of the weld metal for the samples: a) W6N, b) W5N, c) W4N, d) W6R, e) W5R, f) W4R.

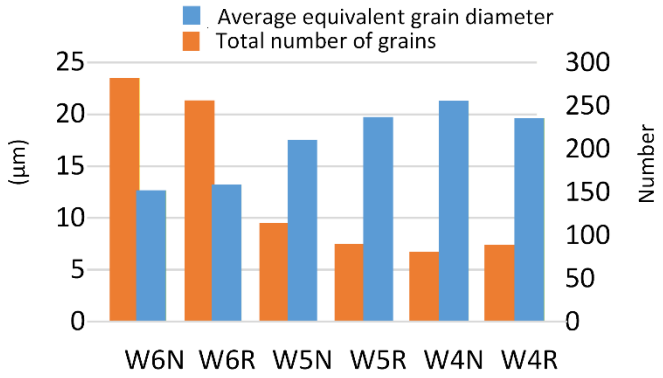


Fig. 12: Average equivalent grain diameter and number of detected grains in the weld metal regions of the different samples.

To further examine the TiB particles responsible for grain refinement, high-magnification SEM imaging and EDS elemental mapping were performed in the weld zone of W6N. Identifying these particles based only on their morphology was difficult because several secondary phases were present in the same region. Fig. 13 shows the weld zone microstructure with the corresponding Al, Ti, Mg, and Fe elemental maps. The Al map shows the matrix, while the Ti map identifies three localized Ti-rich particles within the examined area. The SEM image highlights the positions of these Ti-rich particles. The microstructure consists of grains with an average equivalent diameter of approximately 20 µm, along with bright and dark blade-like phases that are mainly located along the grain boundaries. The EDS results show that the bright, blade-like phases are Fe-rich and contain about 9 wt.% Fe, while the darker phases seem to be Mg-rich phases. The Ti-rich particles might be associated with the grain-refining particles in 6063 filler.

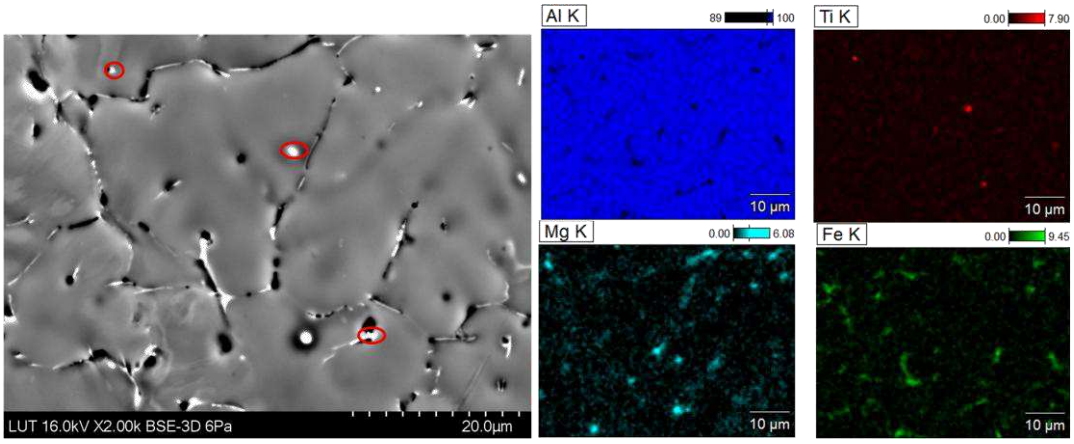


Fig. 13: SEM image and corresponding EDS elemental maps of Al, Ti, Mg, and Fe in the weld zone of sample W6N

Fig. 14 shows SEM images of the weld metal microstructure for the different samples. Fig. 14a to 14c correspond to W6N, W5N, and W4N, respectively, while Fig. 14d presents a higher-magnification image of the weld metal region in W4N. In all samples, intermetallic phases are observed within the matrix, at the boundaries, and in the inter-dendritic regions. The morphology and amount of these phases vary with the filler material used. Fig. 14a shows the weld metal produced by the 6063 filler. This filler has a chemical composition closer to that of the 6082 base metal and contains fewer alloying elements than the other two filler wires. As a result, fewer secondary phases were observed inside the grains and along the grain or dendrite boundaries. Fig. 14b shows the weld metal produced with the 5356 filler. According to Table

1, this filler contains approximately 4.5–5.5 wt.% Mg content. During solidification, Mg segregates into the interdendritic regions. Therefore, the narrow dark phases observed in this image are most likely Mg-rich phases formed between the dendrite arms. Fig. 14c shows the weld metal produced with the 4043 filler. This filler contains a high Si content. During solidification, Si-rich phases can segregate in the inter-dendritic regions. Fig. 14d clearly shows the blade-like morphology of these Si-rich phases in the weld metal of W4N. During electropolishing, the aluminum matrix is selectively corroded, while the Si-rich phases remain less affected. As a result, these phases become more visible in the SEM image.

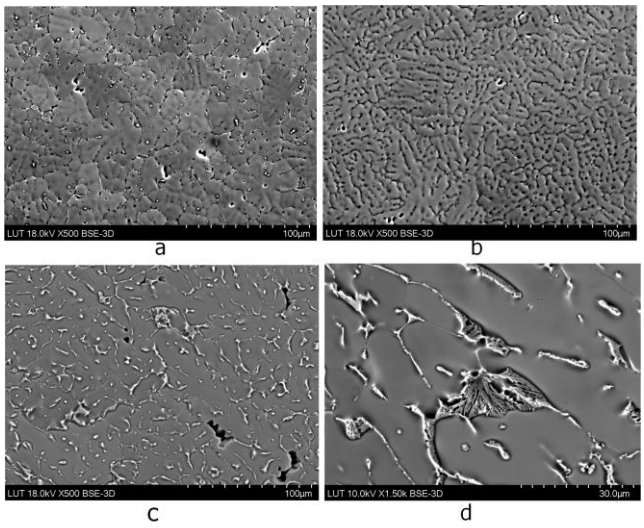


Fig. 14: SEM images of the weld metal microstructure in different samples: a) W6N, b) W5N, c) W4N, and d) higher-magnification image of the W4N weld metal.

Fig. 15 shows an analysis of the differences in alloying element distribution through EDS elemental mapping. The picture presents the distributions of Al, Mg, Si, and Fe in the weld metal microstructures of W6N, W5N, and W4N. The Al maps represent the aluminum matrix, while the Mg, Si, and Fe maps reveal the local segregation of alloying elements and the distribution of secondary phases. In W6N, Mg and Si were relatively dispersed throughout the examined region, with maximum local concentrations of approximately 3.03 wt.% Mg and 4.13 wt.% Si. This relatively limited segregation is due to the lower overall alloying-element content of the 6063 filler. In W5N, a higher Mg concentration was observed in the inter-dendritic regions, reaching approximately 10 wt.% in the most enriched areas. This pronounced Mg segregation is consistent with the high Mg content of the 5356 filler presented in Table 1. The most significant element segregation was observed in W4N, where Si formed a nearly continuous network along the inter-dendritic regions and reached a local concentration of approximately 33 wt.%. This distribution reflects the high Si content of the 4043 filler and supports the identification of the blade-like phases observed in the corresponding SEM image as Si-rich constituents. Localized Fe enrichment was also detected in all three weld metals, with the strongest local enrichment observed in W4N. Overall, the EDS maps confirm that filler composition strongly influenced the amount and distribution of segregated alloying elements and secondary phases in the weld metal.

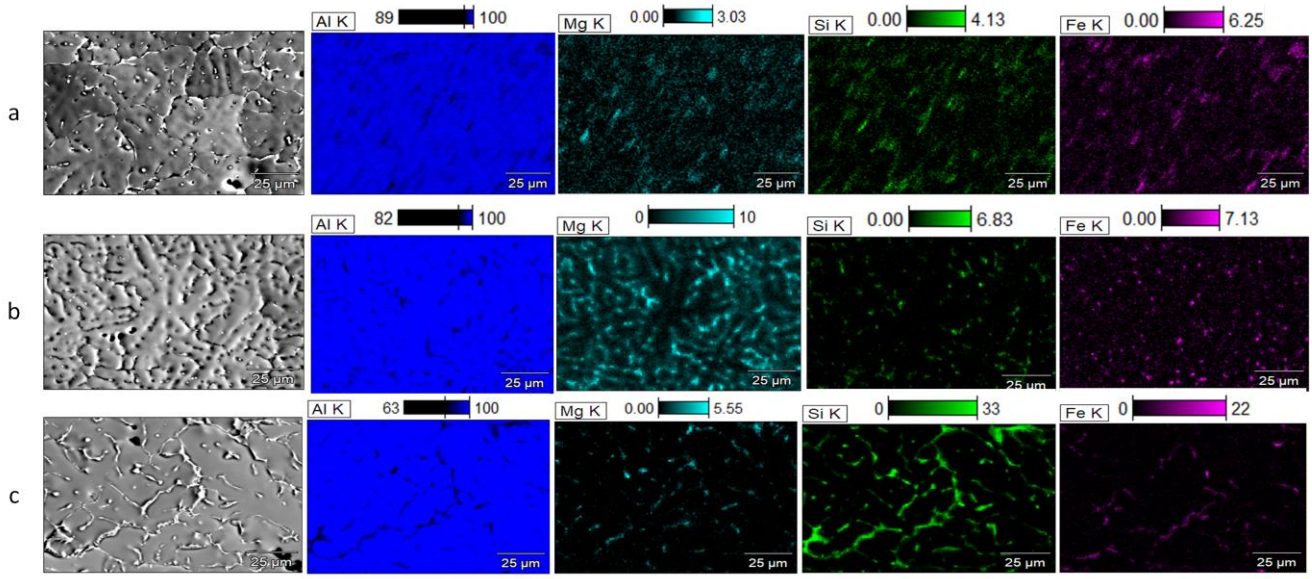


Fig. 15: SEM images and corresponding EDS elemental maps showing the distributions of Al, Mg, Si, and Fe in the weld metal of a) W6N, b) W5N, and c) W4N.

Fig. 16a presents the XRD patterns obtained from the 6082-T651 base metal and the weld metals of W6N, W5N, and W4N. Table 5 also summarizes the crystal structures and calculated lattice parameters of the α-Al matrix and the phases identified in the samples. The primary reflections of the face-centered cubic α-Al matrix dominated all diffraction patterns.The lattice parameter of the α-Al matrix was determined using the high-angle reflections because these reflections provide greater sensitivity to small changes in lattice spacing. The calculated lattice parameters were 4.053 Å for the base metal, 4.054 Å for W6N, 4.053 Å for W5N, and 4.044 Å for W4N. The values obtained for the base metal, W6N, and W5N were close to the reported lattice parameter of approximately 4.05 Å for FCC aluminum [21]. A slightly smaller lattice parameter was obtained for W4N. This difference may be associated with the higher Si content of the 4043 filler and the lower Si supersaturated solid solubility in an aluminum matrix. Nevertheless, the calculated lattice parameters remained close to the reference value for α-Al, confirming that the FCC matrix structure was preserved in all investigated samples.

To improve the detection of low-intensity reflections from secondary phases, additional slow-scan XRD measurements were performed at 40 kV and 35 mA. Fig. 16b presents the slow-scan patterns of the three weld metals over the 2θ range of 30–70°. Several weak reflections were detected in addition to the dominant α-Al (111) and (200) peaks. Comparison of the measured peak positions with theoretical reflections calculated from published crystallographic data allowed these low-intensity peaks to be assigned to β-Mg_2Si, β″-Mg_5Si_6, and crystalline Si [21]. Reflections linked to the equilibrium β-Mg_2Si phase were observed in W6N and W5N. This phase was indexed with a cubic crystal structure and a calculated lattice parameter of 6.340 Å. Weak reflections consistent with the metastable β″-Mg_5Si_6 phase were detected in W4N. The β″ phase was indexed using a monoclinic crystal structure with calculated lattice parameters of a = 15.211 Å, b = 3.985 Å, and c = 6.706 Å. The monoclinic angle was fixed at the literature value of β = 105°.

Additional reflections assigned to crystalline Si were observed only in W4N. These reflections were detected at several diffraction angles, as marked in Fig. 16b. The Si phase was indexed with a diamond cubic structure and a calculated lattice parameter of 5.427 Å. The detection of crystalline Si in W4N is consistent with the high Si content of the 4043 filler. It also supports the EDS map results, which showed extensive Si-enriched regions in Fig. 15c.

The calculated lattice parameters of the identified secondary phases were in close agreement with the corresponding literature values [21], supporting the proposed phase assignments.

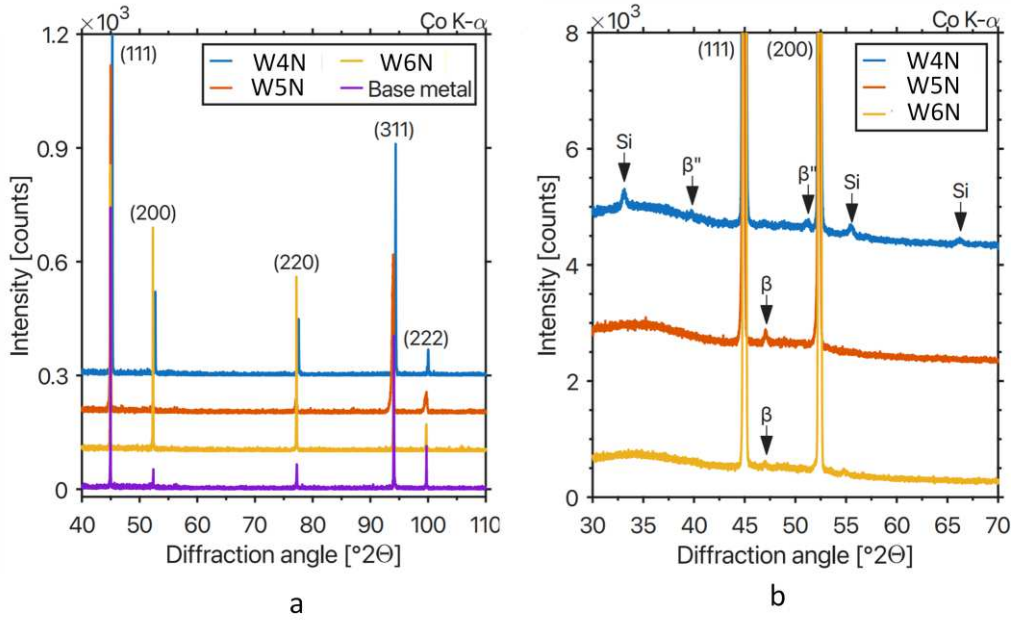


Fig. 16: XRD diffraction patterns of a) base metal, W6N, W5N, and W4N, and b) slow-scan diffraction patterns of W6N, W5N, and W4N within the 2θ range of 30–70°.

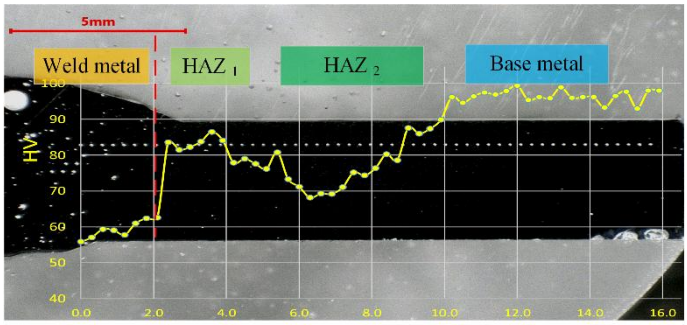
Table 5: The crystal structures and calculated lattice parameters of the detected phases.

Identified phase	**Crystal structure**	**Calculated lattice parameters**
α-Al matrix in 6082-T651	FCC	a = 4.053 ± 0.001 Å
α-Al Matrix in W6N weld metal	FCC	a = 4.054 ± 0.001 Å
α-Al Matrix in W5N weld metal	FCC	a = 4.053 ± 0.002 Å
α-Al Matrix in W4N weld metal	FCC	a = 4.044 ± 0.001 Å
β-Mg_2Si	Cubic	a = 6.340 ± 0.002 Å
β″-Mg_5Si_6	Monoclinic	a*, b*, c*, β*
Si	Diamond cubic	a = 5.427 ± 0.001 Å
*a = 15.211 ± 0.005 Å, b = 3.985 ± 0.005 Å, c = 6.706 ± 0.005 Å, β = 105°		

Fig. 17 shows the Vickers hardness profile across the welded joint and the average hardness values measured in the different regions of the samples. The weld metal is located on the left side of the profile, and the red dashed line indicates the fusion line. Based on the hardness variation, the HAZ can be divided into two different regions, marked as HAZ_1 and HAZ_2. A sharp increase in hardness was observed after crossing the fusion line from the weld metal into HAZ_1. This region is close to the weld metal and was exposed to a relatively high thermal cycle during welding. Since 6082 is a heat-treatable aluminum alloy and contains soluble strengthening precipitates, this region behaves similarly to a supersaturated solid solution zone. The temperature range in this region exceeds the solution annealing temperature, dissolving a portion of the strengthening precipitates into the aluminum matrix. Farther from the fusion line, the hardness decreased compared with HAZ_1. This region was exposed to a lower thermal cycle than HAZ_1, but the temperature was still high enough to affect the precipitates and cause over-aging again. Therefore, the hardness reduction in HAZ_2 can be related to over-aging or coarsening of strengthening precipitates. This softened zone is typical for welded 6xxx

aluminum alloys [7]. After HAZ_2, the hardness gradually increased toward the base metal, where the material was not significantly affected by the welding heat input.

The summarized average hardness values of the weld metal, HAZ_1, HAZ_2, and base metal for all samples are also shown. The base metal showed the highest hardness values, ranging from 105 to 110 HV. Among all samples, W6N and W6R exhibited the lowest weld metal hardness, with average values of 60 HV and 57 HV, respectively.



sample	Hardness (HV)			
	Weld metal	HAZ 1	HAZ2	Base metal
W6N	60	82	71	107
W6R	57	81	71	105
W5N	67	77	70	105
W5R	67	83	75	110
W4N	69	81	70	105
W4R	59	77	70	105

Fig. 17: Vickers hardness profile across the welded joint and average hardness values measured in the weld metal, HAZ1, HAZ2, and base metal for the different samples.

The hardness values in HAZ_1 were generally higher than those in the weld metal and HAZ_2, while HAZ_2 showed a clear softening behavior in all samples. The hardness of HAZ_2 remained in a narrow range of about 70–75 HV. This indicates that the thermal cycle during welding produced a softened region in the heat-affected zone for all welding conditions. Overall, the hardness results show that the welded joints had a non-uniform hardness distribution. The base metal retained the highest hardness, whereas the weld metal and HAZ_2 are the softer regions. The lower hardness of W6N and W6R in the weld metal suggests that the TiB-containing 6063 filler produced a softer weld metal compared with the conventional filler materials, despite strong grain-refining effect observed in the EBSD results.

Fig. 18 shows the tensile properties of the welded samples. The engineering stress–strain curves are presented in Fig. 18a to 18c for the samples welded with 6063, 5356, and 4043 filler metals, respectively. The samples welded with the same filler metal are plotted together in order to compare the CMT and conventional welding process modes. A comparison between the welded joints and the 6082-T651 base metal, Table 2, shows that all welded samples experienced a reduction in mechanical properties after welding. The base metal had a yield strength of 290 MPa, and ultimate tensile strength (UTS) of 340 MPa. In comparison, the welded samples showed yield strengths of 146–165 MPa and UTSs of 205–262 MPa. The reduction in yield strength was significant for all welded samples. The yield strength of the

welded joints was 50–57% of that of the base metal. However, the yield strength values of all welded samples remained in a relatively narrow range. The highest yield strength was obtained for W5R, and the lowest yield strength was measured for W6R. Among all welded joints, W6R showed the highest UTS reduction, almost 70% of the base metal UTS. The yield strength and UTS values of the welded samples were observed within a relatively similar range, with a clear reduction compared to the 6082-T651 base metal. Notably, sample W6R exhibited the most significant decrease in UTS.

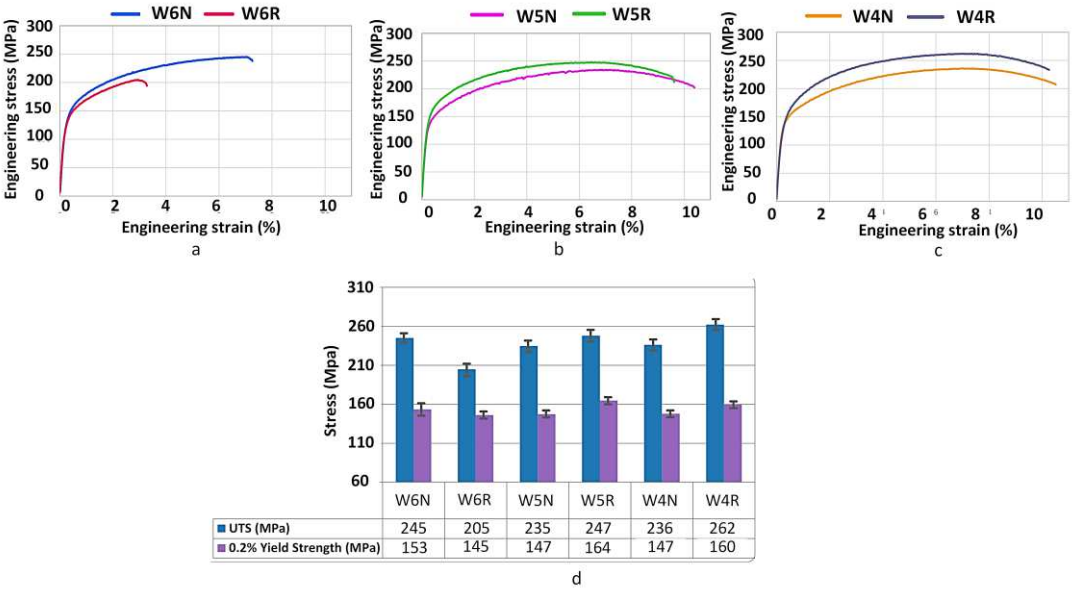


Fig. 18: Tensile properties of the welded samples: engineering stress–strain curves of samples a) W6N and W6R, b) W5N and W5R, c) W4N and W4R, d) average UTS and yield strength.

4. Discussion

The tensile results showed that most welded samples have yield strength and UTS within a comparable range. The primary difference was observed in the deformation capacity. In particular, W6N and especially W6R exhibited lower elongation compared to the other welded samples. This behavior is important because the 6063 filler containing TiB particles produced the finest weld metal grain structure, as shown by the EBSD results. Therefore, an improvement in mechanical performance could be expected. However, the tensile test results showed reduced deformation capacity in these samples, as evidenced by their lower elongation This indicates that grain refinement alone was not sufficient to improve the mechanical behavior of the welded joints. The possible reasons for the lower deformation capacity of samples welded with a heat-treatable filler containing TiB grain-refiner particles were further examined by considering internal defects, fracture location, hardness distribution, and phase formation.

Fig. 19 compares the XCT results of W6N, W6R, and W4N. Fig. 19a and 19b show the detected cavities in W6N with equivalent diameters larger than 0.4 mm and smaller than 0.4 mm, respectively. Fig. 19c and 19d show the corresponding results for W6R. The value of 0.4 mm was selected based on the dimensional limit discussed earlier for individual gas pores in a 4 mm thick plate, according to ISO 10042 [20].

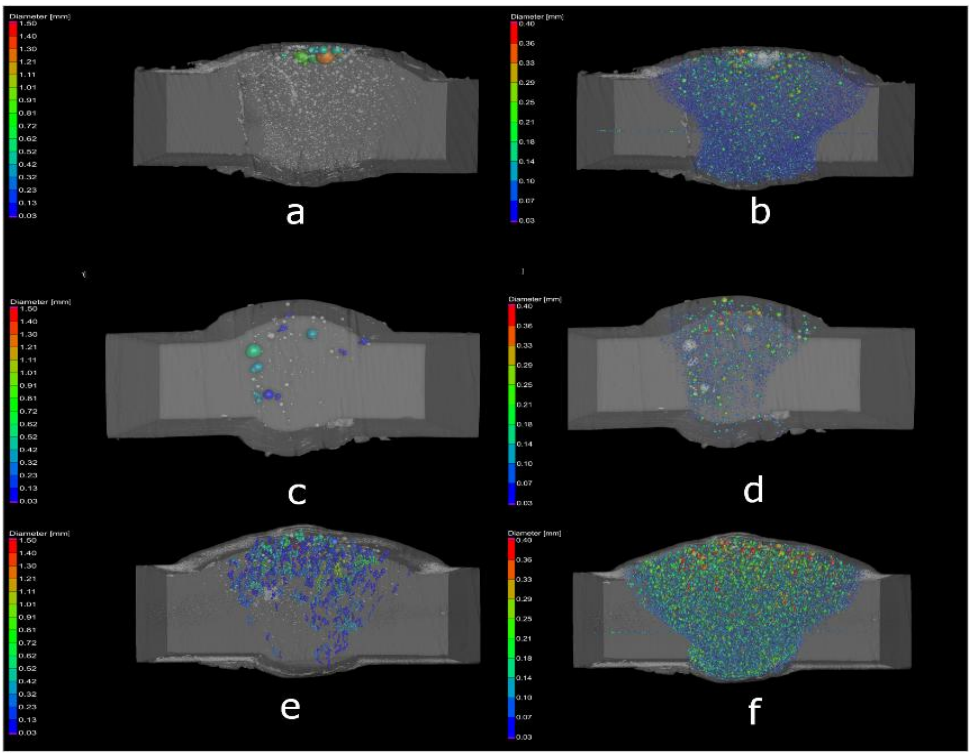


Fig. 19: XCT visualization of internal cavities in W6N, W6R, and W4N. Cavities larger than 0.4 mm in: a) W6N, c) W6R, and e) W4N. Porosities and cavities smaller than 0.4 mm in b) W6N, d) W6R, and f) W4N.

The XCT images show that W6N contained fewer large cavities (diameters > 0.4 mm) than W4N. In contrast, W4N showed a higher number of detected internal cavities in the weld metal region. The number of small cavities below 0.4 mm was also high in both W6N and W6R samples, but W4N showed a higher distribution of these features.

Therefore, the XCT results alone do not fully explain the lower deformation capacity of W6N. Although W4N had more detected cavities than W6N and W6R, the elongation of W4N was higher. This suggests that the total number of detected cavities, especially small cavities below 0.4 mm, was not the only factor controlling the tensile behavior. For this reason, the fracture location and local strain distribution were further investigated using digital image correlation.

Fig. 20 shows the DIC strain maps obtained immediately before fracture for the different welded samples. The images in Fig. 20a to 20f correspond to W6N, W6R, W5N, W5R, W4N, and W4R, respectively. The weld bead region is marked in each image to indicate the weld position relative to local strain and fracture. A clear difference can be observed between the samples welded with the 6063 TiB-containing filler and those welded with the conventional filler materials. In W6N and W6R, the strain was localized to a narrow region near the weld bead and fusion line. These two samples also fractured in this region with high local strain. In contrast, W5N, W5R, W4N, and W4R showed higher local strain farther from the weld bead, in the HAZ. These samples fractured away from the weld metal.

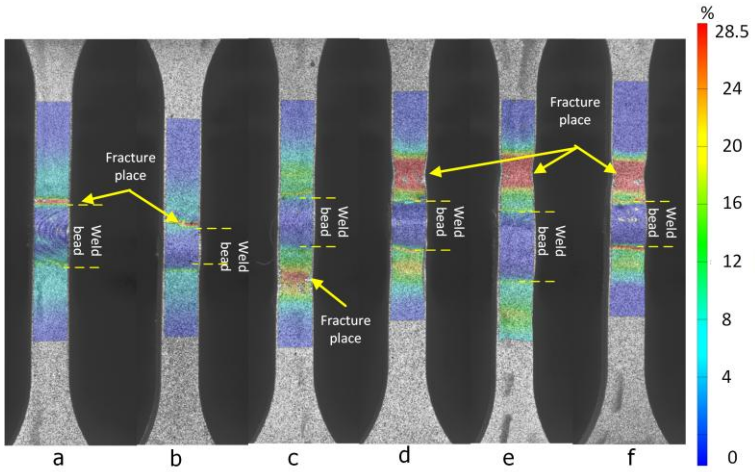


Fig. 20: DIC strain maps before fracture for the welded samples: a) W6N, b) W6R, c) W5N, d) W5R, e) W4N, and f) W4R.

Eventually, for W6N and W6R, the localized strain band developed close to the fusion line, suggesting that this region acts as the weakest part of the joint where these samples showed the lowest hardness in the weld metal. Therefore, the reduced weld metal hardness and potentially lower strength likely promoted local strain concentration, deformation capacity reduction, and early fracture near the fusion line.

To examine the fracture location of W6N and W6R in more detail, cross-sectional observations of the fractured samples were performed, as shown in Fig. 21. The results confirmed that the fracture occurred close to the fusion line and within the weld metal side in both samples. In Fig. 21b, a large pore can also be observed near the fracture path. This pore was also detected in the XCT results shown earlier. Such a defect may have acted as a preferential site for fracture initiation because porosity reduces the effective load-bearing area of the weld.

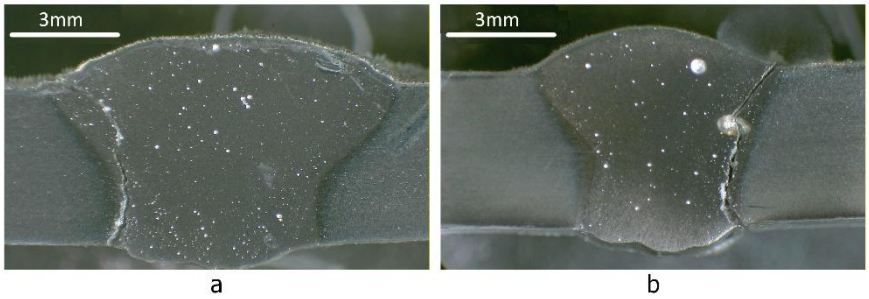


Fig. 21: Cross section of the fracture path in the samples: a) W6N and b) W6R.

Another important observation in Fig. 21a and 21b is that the crack did not propagate through the center of the weld metal. This can be related to the weld reinforcement geometry. The central part of the weld has a larger cross-sectional area due to reinforcement, which can reduce the local stress by increasing the load-bearing area. As a result, the crack path turned back toward the fusion-line region instead of propagating through the weld center. The crack also did not continue into the base metal. This is consistent with the hardness results, which showed that the weld metal in W6N and W6R had lower hardness than the adjacent HAZ and base material. Therefore, the crack preferentially propagated along the weaker region close to the fusion line, where the local resistance to deformation and fracture was lower. For the other

samples, although porosity and shrinkage cavities were also detected by XCT, no fracture occurred in the weld metal. This suggests that their weld metals had sufficient local strength to avoid yielding and fracturing near the fusion line. Instead, fracture occurred in the softened region of the HAZ, which is typical for heat-treatable aluminum alloys welding [22]. Therefore, the DIC results support the conclusion that the poor deformation capacity of W6N and W6R was mainly related to local weakening of the weld region, rather than only to the total amount of porosity.

To investigate the reason for the lower mechanical performance of the samples welded with the 6063 filler, XRD analysis was performed on different regions of W6N. The purpose of this analysis was to evaluate the presence of strengthening phases. Since the main strengthening precipitates in 6xxx-series aluminum alloys typically exist at the nanoscale, direct observation of their morphology requires high-resolution transmission electron microscopy (TEM). However, visual morphological characterization of such nanoscale precipitates was beyond the scope of the present study. Therefore, high-resolution XRD analysis was used as a complementary method to detect possible phase-related differences between the weld metal and HAZ regions.

Fig. 22 shows the XRD patterns obtained from different regions of the W6N sample, including the weld metal, weld boundary (WB, corresponding to the mushy zone), HAZ_1, and HAZ_2. The scans were recorded using Co Kα radiation in the 2θ range of 40–70°, with particular attention to the region where weak reflections from strengthening precipitates were expected. The identified β″-Mg_5Si_6 phase is known as the primary strengthening precipitate in 6xxx-series aluminum alloys, whereas β-Mg_2Si represents the equilibrium end product of the precipitation process [21, 22].

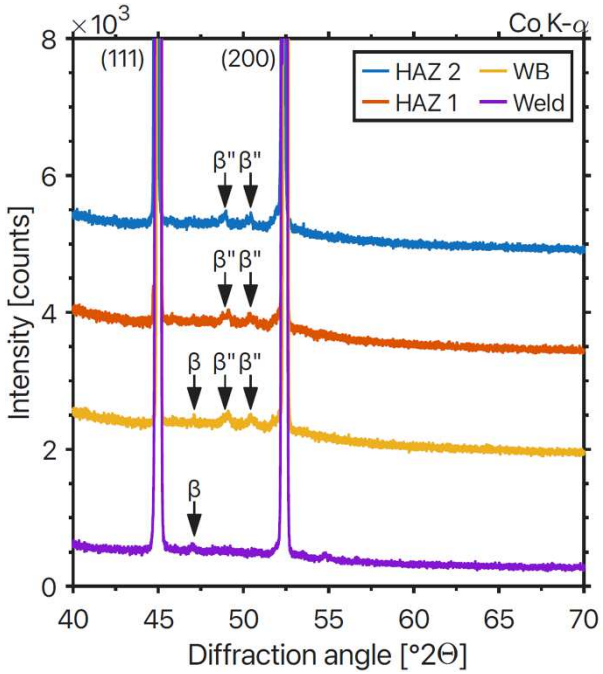


Fig. 22: XRD patterns of the weld metal, weld boundary, HAZ1, and HAZ2 regions in W6N, recorded in the 2θ range of 40–70°.

The weld metal area showed only reflections related to β-Mg_2Si, while the HAZ regions displayed reflections indicative of β″-Mg5Si6. The mushy zone or weld boundary region showed reflections from both β-Mg_2Si and β″-Mg_5Si_6. This indicates that the phase constitution

changed across the weld cross-section, from the weld metal toward the HAZ. No significant difference was observed between the diffraction patterns from HAZ_1 and HAZ_2, as both regions displayed similar β″-Mg_5Si_6 reflections. This suggests that the phase transformation remained relatively consistent across the HAZ regions examined.

The absence of detectable β″-Mg_5Si_6 reflections in the weld metal is aligned with the lower hardness measured in this region. Since β″-Mg_5Si_6 is the primary strengthening precipitate in 6xxx-series aluminum alloys, its absence or difficulty in detecting it in the weld metal suggests a reduced precipitation strengthening contribution. This provides more evidence that the weld metal in the W6 samples was mechanically weaker than the adjacent HAZ and base material.

Fig. 23 shows the fracture surfaces of the W6N and W6R samples. Fig. 23a and 23b correspond to W6N and W6R, respectively, and Fig. 23c shows a higher magnification of the marked region in Fig. 23b. A common feature in both W6N and W6R is the presence of many spherical pores on the fracture surface. In addition, the fracture surfaces are covered with numerous dimples, indicating that the fracture involved a ductile mechanism.

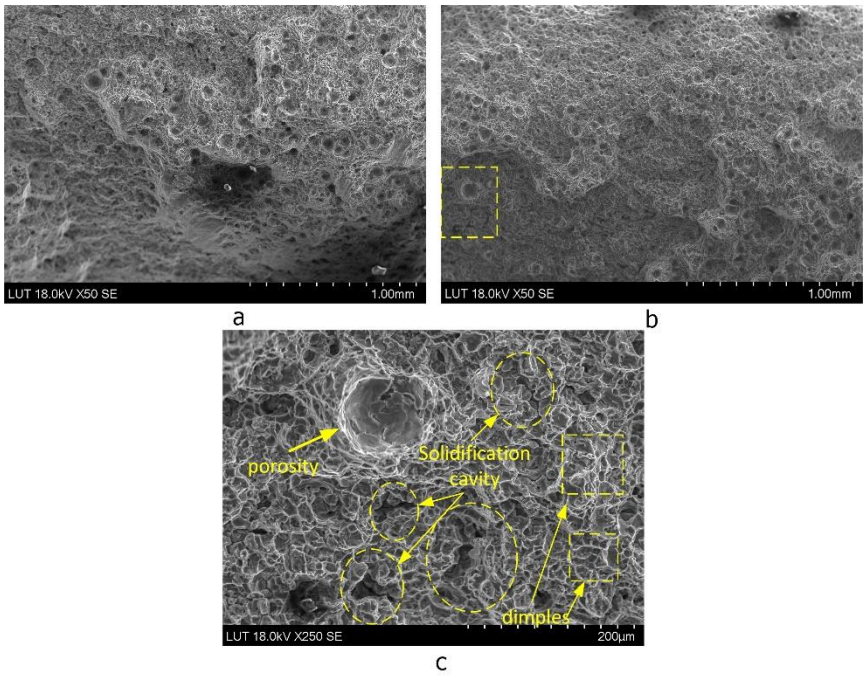


Fig. 23: SEM images of fracture surface observations of the samples a) W6N, b) W6R, and c) a higher-magnification image of the marked region in 23b.

The higher-magnification image in Fig. 23c shows one spherical pore and many irregularly shaped cavities. The spherical cavities are typical of gas porosity, while the irregular cavities are more characteristic of shrinkage cavities [23–25]. These observations support the results obtained from XCT, DIC, and hardness measurements. The weld metal in the W6 samples had relatively low hardness and contained a high number of imperfections, including gas pores and shrinkage-related cavities. Therefore, the combination of a weak weld metal region and internal imperfections led to earlier fracture compared with other samples. This explains why the W6 samples, especially W6R, showed lower elongation and strength properties despite the refined grain structure produced by the TiB-containing filler.

5. Conclusions

In this study, 6082-T651 plates were welded using three different filler wires, including a heat-treatable 6063 filler containing TiB particles and two conventional aluminum filler metals, 5356 and 4043. The effects of filler chemistry and CMT welding mode on weld metal microstructure, internal defects, hardness distribution, and tensile performance were investigated. The main conclusions are as follows:

- The 6063 filler containing TiB particles produced the most refined weld metal grain structure. EBSD analysis showed that the W6N and W6R samples had a much smaller average grain diameter and a higher number of detected grains compared with the samples welded with the conventional 5356 and 4043 fillers. This confirms the strong grain-refining effect of the TiB-containing filler. However, the effect of the CMT welding mode on grain refinement was relatively limited compared with the effect of TiB particles.
- The influence of the CMT welding process depended strongly on the filler material. For the 5356 and 4043 filler metals, the CMT mode improved the UTS compared with the corresponding normal welding conditions. In contrast, the simultaneous use of the CMT welding process and the TiB-containing 6063 filler did not improve the mechanical performance. The W6R sample showed the lowest UTS and the lowest elongation among all welded samples.
- All welded joints showed a reduction in mechanical properties compared with the 6082-T651 base metal. The yield strength values of the welded samples were within a relatively narrow range and were lower than those of the base metal. The main difference between the samples was observed in elongation and overall tensile response.
- Hardness measurements showed a non-uniform hardness distribution across the welded joints. The base metal retained the highest hardness, while the weld metal and HAZ_2 were the softer regions. The W6N and W6R samples showed the lowest weld metal hardness. This local softening of the weld metal leads to high local strain in a narrow area and premature fracture near the fusion line. W6N and W6R fractured close to the fusion line and mainly from the weld-metal side, while the other samples fractured in the heat-affected zone away from the weld metal. This behavior can be related to the low hardness of the weld metal in W6N and W6R, the limited presence of strengthening precipitates in the weld metal, and the high strain localization in a very narrow region near the fusion line. These factors reduced the local deformation capacity of the weld region.
- XCT analysis showed that internal cavities were present in the welded joints. However, the total number of detected cavities alone did not fully explain the behavior under tensile load. For example, W4N contained more detected cavities than W6N, but showed higher elongation. This indicates that defect size, morphology, location, and the local strength of the weld region are more important than pore count alone.

Acknowledgements

The authors would like to thank Antti Heikkinen from the Metallography Laboratory, Antti Kähkönen from the Welding Technology Laboratory, and Olli-Pekka Pynnönen from the Steel Structures Laboratory for their valuable technical assistance and laboratory support during the experimental work.

Data Availability Statement:
The data that support the findings of this study are available from the corresponding author, Amir Khodabakhshi, upon reasonable request.

Author Contributions

Conceptualization: Amir Khodabakhshi.
Experimental work: Amir Khodabakhshi and Sakari Penttilä
Data analysis: Amir Khodabakhshi, Shahriar Afkhami, Hamidreza Rohani Raftar, Ville Laitinen
Writing original draft: Amir Khodabakhshi.
Review & editing: Shahriar Afkhami. Hamidreza Rohani Raftar, Ville Laitinen
Project administration: Tuomas Skriko.
Funding acquisition: Tuomas Skriko.
All authors have read and agreed to the published version of the manuscript.

Competing Interests
The authors declare no competing interests.

Funding
This work was financially supported by the Laboratory of Welding Technology at LUT University, Finland.

References:

1. Tunc O, Kacar I, Ozturk F (2021) Investigation of forging performance for 6082. The International Journal of Advanced Manufacturing Technology 117:1645–1661. https://doi.org/10.1007/s00170-021-07726-8
2. Alzahrani B, Abd El-Aty A, Elatriby SA, et al (2024) A Modified Johnson Cook Model-Based Kalman Filter Method to Determine the Hot Flow Behavior of Sustainable 6082 Al Alloy. Materials 17:5169. https://doi.org/10.3390/ma17215169
3. Bansal A, Pabla BS, Vettivel SC (2018) Effect of TIG Welding Process Parameters on Tensile behavior of 5XXX and 6XXX series Aluminium Alloys: A Review. Research Journal of Engineering and Technology 9:1. https://doi.org/10.5958/2321-581X.2018.00001.6
4. Chen X, Tang S, Xie W, et al (2024) Effect of Heat Input on the Microstructure and Mechanical Properties of 6060 Aluminum Alloy/Galvanized STEEL MIG Welding–Brazing Joints. Transactions of the Indian Institute of Metals 77:1589–1596. https://doi.org/10.1007/s12666-024-03277-0
5. Cui S, Liu X, Zhang W, et al (2025) Effect of Welding Current on Molten Pool Dynamics and Microstructure in MIG Welding of 6063-T6 Aluminum Alloy. JOM 77:9023–9032. https://doi.org/10.1007/s11837-025-07639-x
6. de Salazar JMG, Ureña A, Villauriz E, et al (1999) TIG and MIG welding of 6061 and 7020 aluminium alloys. Microstructural studies and mechanical properties. Welding International 13:293–295. https://doi.org/10.1080/09507119909447381
7. Khodabakhshi A, Havia J, Afkhami S, et al (2025) The effects of different weld zone characteristics on mechanical properties and fracture behavior of MIG welded 5754, 5083, and 6082 aluminum alloys. Welding in the World. https://doi.org/10.1007/s40194-025-02180-6
8. Himarosa RA, Mudjijana, Adi RK, et al (2022) Simultaneous Double-Sided Metal Inert Gas Welding of 5052 Aluminum Alloy T-Joints. Materials Science Forum 1067:53–59. https://doi.org/10.4028/p-t0072n
9. Schempp P, Cross CE, Pittner A, Rethmeier M (2013) Influence of Solute Content and Solidification Parameters on Grain Refinement of Aluminum Weld Metal. Metallurgical and Materials Transactions A 44:3198–3210. https://doi.org/10.1007/s11661-013-1649-3
10. Babu NK, Pan D, Sun Z, et al (2012) Effect of titanium–boron additions on grain refinement of 2219 gas tungsten arc welds. Science and Technology of Welding and Joining 17:386–393. https://doi.org/10.1179/1362171812Y.0000000020
11. Schempp P, Rethmeier M (2015) Understanding grain refinement in aluminium welding. Welding in the World 59:767–784. https://doi.org/10.1007/s40194-015-0251-2
12. Kirkbakk KM, Marhaug N, Kvam-Langelandsvik G, Werenskiold JC (2023) Grain refinement of aluminium welds by Ti, TiB2, and TiC filler wire inoculation. The International Journal of Advanced Manufacturing Technology 128:5117–5127. https://doi.org/10.1007/s00170-023-12199-y

13. Rykała J (2014) Robotic welding of thin wall components made of 6xxx and 2xxx series aluminium alloys using low-energy methods. Welding International 28:333–338. https://doi.org/10.1080/09507116.2012.708486

14. Elrefaey A, Ross NG (2015) Microstructure and Mechanical Properties of Cold Metal Transfer Welding Similar and Dissimilar Aluminum Alloys. Acta Metallurgica Sinica (English Letters) 28:715–724. https://doi.org/10.1007/s40195-015-0252-6

15. Liu YB, Sun QJ, Sang HB, Feng JC (2015) Microstructure and mechanical properties of cold metal transfer welded aluminium/nickel lap joints. Science and Technology of Welding and Joining 20:307–312. https://doi.org/10.1179/1362171815Y.0000000011

16. Wei W, Sun Y, Zhang C, et al (2025) Effect of CMT and MIG Welding on Microstructure and Mechanical Properties of Al-Zn-Mg-Cu-Er-Zr Alloy. Materials 18:4688. https://doi.org/10.3390/ma18204688

17. Cornacchia G, Cecchel S, Panvini A (2018) A comparative study of mechanical properties of metal inert gas (MIG)-cold metal transfer (CMT) and fiber laser-MIG hybrid welds for 6005A T6 extruded sheet. The International Journal of Advanced Manufacturing Technology 94:2017–2030. https://doi.org/10.1007/s00170-017-0914-9

18. Grzybicki M, Jakubowski J (2013) Comparative tests of steel car body sheet welds made using CMT and MIG/MAG methods. Welding International 27:610–615. https://doi.org/10.1080/09507116.2011.606147

19. Rohani Raftar H, Khodabakhshi A, Havia J, et al (2025) Experimental and numerical study of welding-induced deformation and residual stress in 6082 aluminum: Model validation and process design guidance. Mater Des 255:114193. https://doi.org/10.1016/j.matdes.2025.114193

20. International Organization for Standardization (2018) Welding — Arc-welded joints in aluminium and its alloys — Quality levels for imperfections. Geneva, Switzerland. ISO 10042:2018.

21. RAVI C (2004) First-principles study of crystal structure and stability of Al-Mg-Si (Cu) precipitates. Acta Mater 52:4213–4227. https://doi.org/10.1016/j.actamat.2004.05.037

22. Afkhami S, Khodabakhshi A, Havia J, et al (2026) Experimental-numerical insights into heat-affected zone failure of welded aluminum alloys. Welding in the World. https://doi.org/10.1007/s40194-026-02394-2

23. Chen Y, Chen X, Zhang Q, et al (2022) Numerical Modeling of Welding Porosity Formation and Dendrite Growth of 6xxx Aluminum Alloys. JOM 74:2428–2436. https://doi.org/10.1007/s11837-022-05213-3

24. Samuel AM, Samuel E, Songmene V, Samuel FH (2023) A Review on Porosity Formation in Aluminum-Based Alloys. Materials 16:2047. https://doi.org/10.3390/ma16052047

25. Ardika RD, Triyono T, Muhayat N, Triyono (2021) A review porosity in aluminum welding. Procedia Structural Integrity 33:171–180. https://doi.org/10.1016/j.prostr.2021.10.021